Equilibrium Calculation with Toroidal Flow in NIMEQ

by

Tyler Markham

A thesis submitted to the Graduate Faculty of
Auburn University
in partial fulfillment of the
requirements for the Degree of
Master of Science

Auburn, Alabama
August 5, 2018

Keywords: Isothermal, Toroidal, Grad-Shafranov, Bernoulli, Flow, NIMEQ

Approved by

Luca Guazzotto, Associate Professor of Physics
David Maurer, Professor of Physics
Yu Lin, Alumni Professor of Physics
George Flowers, Dean of the Graduate School and Professor of Mechanical Engineering

Abstract

The focus of this work is to demonstrate the importance of incorporating toroidal rotation in calculating tokamak-like equilibria with axisymmetry. Specifically, this work will focus on showing the impact toroidal flow had on the particle density, poloidal magnetic flux, and toroidal current density. We utilize the analytical form of the thermal pressure, for purely toroidal flow in the isothermal limit. Modifications to NIMRODs equilibrium solver, NIMEQ, are made to integrate toroidal flow and to ensure NIMEQ's solution fields are self-consistent. The modifications to NIMEQ are benchmarked by the code FLOW created by L. Guazzotto. Results for a low-β and high-β tokamak like equilibrium are shown. It is found that for both equilibria the peak particle density significantly shifts and the addition of large rotational inertia causes the toroidal current to be pushed outward. Shift in the max poloidal magnetic flux is found to only be significant for the high-β equilibrium, due to toroidal flow's influence on the now dominant thermal pressure. It is expected that the addition of poloidal flow will even further alter equilibrium configurations.

Table of Contents

List of Figures

List of Tables

Chapter 1

Introduction

To date, tokamak devices are the leading candidates for a controlled thermonuclear fusion reactor. However, most transport models neglect flow in the basic equilibrium. Though it is commonly known that poloidal flow is often dampened, toroidal flows are often not. In fact, neutral beam injection, which has become a very common way to heat plasma in tokamaks, can give rise to toroidal velocities up to the ion sound speed [4]. Such high toroidal flow will likely cause significant changes to equilibrium configurations due to the large rotational inertia and sub-super sonic flow transitions [3].

The overarching goal of this thesis is to show the significance of including self-consistent flow in equilibrium calculations for axisymmetric toroidal plasmas with circular poloidal cross-sections. This is done by creating a low-β and a high-β tokamak like static equilibrium, where β is the ratio of thermal and magnetic pressure, and increasing the toroidal Mach number M_ϕ while fixing the rest of the equilibrium parameters.

Regardless of whether the equilibrium is static or steady-state, the Grad-Shafranov equation used must generally be solved numerically [8]. In this thesis we derive the Ideal MHD Grad-Shafranov Bernoulli system of equations for arbitrary flow and show that, in the case of isothermal toroidal flow, the thermal pressure and particle density have analytical forms that reduce the Grad-Shafranov-Bernoulli system of equations to a steady-state form of the static Grad-Shafranov equation. We show the results of numerically generated equilibria for low and high β tokamak like configurations. The numerically generated equilibria will be calculated using the NIMROD (Non-Ideal MHD with Rotation) code's Ideal MHD equilibrium solver, NIMEQ [1]. Previously, NIMEQ solved the static Grad-Shafranov equation, but has since been

modified to incorporate isothermal toroidal flow as a first step to implementing arbitrary flow. The FLOW code developed by L. Guazzotto, which was made to study fixed boundary equilibria with arbitrary flows is used as a benchmark for NIMEQ's new functionality [3]. Percent difference is plotted versus toroidal radius to show how well the two codes compare.

Chapter 2

Theoretical Framework

2.1 General Formulation for Grad-Shafranov-Bernoulli System of Equations

The Ideal MHD equations for arbitrary flow at equilibrium are as follows:

$$\nabla \cdot (\rho \mathbf{v}) = 0 \tag{2.1}$$

$$\rho \mathbf{v} \cdot \nabla \mathbf{v} = \mathbf{J} \times \mathbf{B} - \nabla p \tag{2.2}$$

$$\nabla \cdot \mathbf{B} = 0 \tag{2.3}$$

$$\mu_0 \mathbf{J} = \nabla \times \mathbf{B} \tag{2.4}$$

$$\nabla \times (\mathbf{v} \times \mathbf{B}) = 0, \tag{2.5}$$

where ρ is the mass density, $\mathbf{v}$ is the flow velocity, $\mathbf{J}$ is the current density, $\mathbf{B}$ is the magnetic field, p is the isotropic thermal pressure, and μ_0 is the vacuum magnetic permeability. The MHD closure relation is defined by the relationship below,

$$\mathbf{v} \cdot \nabla \left(\frac{p}{\rho^\gamma} \right) = 0, \tag{2.6}$$

where γ is the ratio of heat capacities. We will use the cylindrical coordinates (R,Z,ϕ), where R is the major radius, Z is the distance above/below the midplane of the torus, and ϕ is the toroidal angle. For toroidal geometry, it is convenient to write the magnetic field in the form $\mathbf{B} = \mathbf{B_p} + \mathbf{B}_\phi$, where $\mathbf{B_p}$ is the poloidal magnetic field and $\mathbf{B}_\phi$ is the toroidal magnetic field, which describes the short and long way around the torus, respectively. Following the procedure

in Appendix A, it can be shown that the magnetic field can be written as

$$\mathbf{B} = \nabla\psi \times \nabla\phi + RB_\phi \nabla\phi, \tag{2.7}$$

where $\hat{\phi} = R\nabla\phi$, $\psi = \psi_p/2\pi$, and ψ_p is the poloidal magnetic flux. Note that (2.7) is indeed divergence free as is required by (2.3). Moreover, (2.7) outlines a very convenient orthogonal basis set: $\nabla\psi$, $\nabla\psi \times \nabla\phi$, and $\nabla\phi$.

The derivation for the Grad-Shafranov equation with arbitrary flow is analogous to the static case, with the notable exception that we must first characterize the flow velocity $\mathbf{v}$. As outlined in Appendix B, our flow velocity can be determined by first proving that $\mathbf{v} \cdot \nabla\psi = 0$, which implies that the flow velocity does not have a $\nabla\psi$ component. Hence, the flow velocity will take a form analogous to that of the magnetic field. Substitution of $\mathbf{v}$ into the continuity equation (2.1) allows us to find the poloidal flow velocity. Finally inserting this new version of $\mathbf{v}$ into (2.5) gives us the final form for the flow velocity

$$\mathbf{v} = \frac{\Phi(\psi)}{\sqrt{\mu_0}\rho}\mathbf{B} + R^2\Omega(\psi)\nabla\phi, \tag{2.8}$$

where $\Phi(\psi)$ and $\Omega(\psi)$ are free functions. Note that $\Phi(\psi)$ helps determine the field aligned component of the flow velocity. Upon inspection of (2.8), we can see that it is never possible to have a purely poloidal flow, regardless of the choice of $\Phi(\psi)$ [3]. This is due to the fact that the poloidal flow inherently influences v_ϕ, where v_ϕ is given by

$$v_\phi = \frac{\Phi(\psi)}{\sqrt{\mu_0}\rho}\mathbf{B}_\phi + R\Omega(\psi). \tag{2.9}$$

Now that the velocity has been determined, we can place $\mathbf{v}$ into our closure relationship (2.6) to get the more useful relationship

$$S(\psi) = \frac{p(R,\psi)}{\rho(R,\psi)^\gamma} = \frac{p_0(\psi)}{D(\psi)^\gamma}, \tag{2.10}$$

where $S(\psi)$ is the specific entropy for $\gamma = \frac{5}{3}$ and the specific temperature for $\gamma = 1$, while $D(\psi)$ and $p_0(\psi)$ are free functions with units of mass density and pressure, respectively. Here, it is necessary to distinguish between the thermal pressure, mass density, $p_0(\psi)$, and $D(\psi)$. In the static case the thermal pressure and mass density are free functions, but that is not the case in the presence of flow. Rotational inertia inside the torus also implies an R dependence. We will address the implications of the closure in greater detail in the next section.

Now that our flow velocity and closure relationship have been established, all that is left to find, before we deal with the momentum equation, is the current density. This can be done by simply substituting our expression for the magnetic field (2.7) into Ampere's Law, which yields

$$\mathbf{J} = \frac{1}{\mu_0}\nabla\left(RB_\phi\right) \times \nabla\phi - \Delta^*\psi\nabla\phi, \tag{2.11}$$

where $\Delta^*\psi = R^2\nabla\cdot(\nabla\psi/R^2)$. Note that J_ϕ is identical to its static form. However, as will be mentioned in the next chapter, the centrifugal force will play a role in shaping the current density profile along the midplane.

The final step is to take our flow velocity (2.8), magnetic field (2.7), and current density (2.11) and plug them into the $\nabla\phi$, $\mathbf{B}$, and $\nabla\psi$ components of the momentum equation (2.2). After a significant amount of algebra, as shown in Appendixes B and C, the $\nabla\phi$ and $\mathbf{B}$ components of the momentum equation bear the following results:

$$RB_\phi = \frac{F(\psi) + \sqrt{\mu_0}R^2\Phi(\psi)\Omega(\psi)}{1 - \Phi(\psi)^2/\rho} \tag{2.12}$$

$$\frac{1}{2\mu_0}\left(\frac{\Phi(\psi)B}{\rho}\right)^2 - \frac{1}{2}R^2\Omega(\psi)^2 + \left(\frac{\gamma}{\gamma-1}\right)S(\psi)\rho^{\gamma-1} = H(\psi). \tag{2.13}$$

Equation (2.12) indicates that $F(\psi) = RB_\phi$ only when there is no poloidal flow, or when $\Phi(\psi) = 0$. The $\mathbf{B}$ component of the momentum equation (2.13) yields a Bernoulli equation that we can use to solve for the mass density in terms of free functions, ψ, $\nabla\psi$, and R. Note that there is a singularity at $\gamma = 1$, or when our closure (2.10) becomes isothermal. This will be a key topic in the next section.

Lastly, we take the $\nabla\psi$ component of the momentum equation and regroup its terms such that the entire RHS of the equation is determined by free functions, constants and R. Following the procedure in Appendix D, the final form of the Grad-Shafranov equation with arbitrary flow is given by

$$\frac{1}{\mu_0}\nabla\cdot\left[\left(1-M_{Ap}^2\right)\left(\frac{\nabla\psi}{R^2}\right)\right] = -\frac{B_\phi}{\mu_0 R}\frac{dF(\psi)}{d\psi} - \frac{\mathbf{v}\cdot\mathbf{B}}{\sqrt{\mu_0}}\frac{d\Phi(\psi)}{d\psi} \\ -\rho R v_\phi\frac{d\Omega(\psi)}{d\psi} - \rho\frac{dH(\psi)}{d\psi} + \frac{\rho^\gamma}{\gamma-1}\frac{dS(\psi)}{d\psi}, \tag{2.14}$$

where $M_{Ap} = \Phi(\psi)/\sqrt{\rho}$ is the poloidal Alfvénic Mach number. Equation (2.14) has also been derived several times throughout the relevant literature [2, 3, 4, 5, 6]. Note that when $\Omega(\psi) = 0$ and $\Phi(\psi) = 0$, (2.14) returns to the static Grad-Shafranov equation.

2.2 Equilibrium with Toroidal Flow in the Isothermal Limit

The general formulation (2.14) requires considerable input in the form of free functions, as well as a solution for $\rho(R,\psi)$ obtained from the Bernoulli equation (2.13). Since NIMROD's equilibrium solver, NIMEQ, assumes a static equilibrium, the LHS (left-hand-side) of the Grad-Shafranov equation is just $\Delta^*\psi$. Equipping NIMEQ with the ability to calculate equilibria with arbitrary flow would require modifications to several low and high level functions. Ergo, we will make two simplifications to (2.14) as a proof of concept for self-consistent flow in NIMEQ.

Firstly, we will only consider the case of purely toroidal flow. Setting $\Phi(\psi) = 0$ and substituting in the derivative of $H(\psi)$ with respect to ψ reduces (2.13) and (2.14) down to

$$\left(\frac{\gamma}{\gamma-1}\right)S(\psi)\rho^{\gamma-1} - \frac{1}{2}R^2\Omega(\psi)^2 = H(\psi) \tag{2.15}$$

$$\Delta^*\psi = -F(\psi)\frac{dF(\psi)}{d\psi} - \mu_0 R^2\left[\rho\left(R^2\Omega(\psi)\frac{d\Omega(\psi)}{d\psi} + \frac{dH(\psi)}{d\psi}\right) - \frac{\rho^\gamma}{\gamma-1}\frac{dS(\psi)}{d\psi}\right]. \tag{2.16}$$

Note that the LHS of (2.16) is now identical to the static case, which means the LHS routines in NIMEQ will no longer have to be altered. However, we would still need to solve for ρ before

any RHS (right-hand-side) routines could take place. Fortunately, for purely toroidal flow, we can solve for the mass density analytically.

We define a nominal mass density $D(\psi) = \rho(R_0, \psi)$ where R_0 is the major radius at the geometric center of the torus [2]. Our closure relation (2.10) requires that the pressure and mass density change together. Hence, as a direct result of our definition for $D(\psi)$, the thermal pressure at $R = R_0$ must also be a free function, which we will denote as $p_0(\psi)$. Since $H(\psi)$ is free, the Bernoulli equation must be equivalent to $H(\psi)$ regardless of toroidal radius. Setting $H(\psi)$ at $R = R_0$ and $H(\psi)$ at any arbitrary R equal to each other and solving for $\rho(R, \psi)$ in terms of the free functions $p_0(\psi)$, $D(\psi)$, and $\Omega(\psi)$, we get the following expression for the mass density:

$$\rho(R, \psi) = D(\psi) \left[1 + \frac{1}{2} \left(R^2 - R_0^2 \right) \Omega(\psi)^2 \left(\frac{\gamma - 1}{\gamma} \right) \frac{D(\psi)}{p_0(\psi)} \right]^{\frac{1}{\gamma - 1}} . \tag{2.17}$$

By inspection we can see that when $\Omega(\psi) = 0$, the mass density is $D(\psi)$. Through the same closure argument we previously made to define $p_0(\psi)$, the thermal pressure must also equal $p_0(\psi)$ in the absence of toroidal flow. Given this information, it's helpful to think of $D(\psi)$ and $p_0(\psi)$ as the static mass density and static thermal pressure.

Lastly, we can simplify (2.16) and (2.17) even further by considering the isothermal limit, or the limit as $\gamma \to 1$. Though at first glance the exponent in (2.17) seems to suggest that a numerical approach is required to take this limit, an analytical limit exists for this expression. Additionally, as previously mentioned, thanks to (2.10), the thermal pressure must have the exact same functional dependence as the mass density. For $\gamma \to 1$, this is easily seen by multiplying both sides of (2.17) by $S(\psi)$. The resulting expressions for mass density and thermal pressure are as follows:

$$\rho(R, \psi) = D(\psi) \exp \left(\frac{p_\omega(\psi)}{p_0(\psi)} \left(\frac{R^2 - R_0^2}{R_0^2} \right) \right) \tag{2.18}$$

$$p(R, \psi) = p_0(\psi) \exp \left(\frac{p_\omega(\psi)}{p_0(\psi)} \left(\frac{R^2 - R_0^2}{R_0^2} \right) \right) , \tag{2.19}$$

where $p_\omega(\psi) = \frac{1}{2}R_0^2 D(\psi)\Omega(\psi)^2$ is the nominal rotational pressure. In the isothermal limit, the thermal pressure and mass density adopt a Gaussian like behavior in R with their static equivalents as their amplitudes.

By substituting (2.10) and (2.18) into (2.16), eventually the Grad-Shafranov equation reduces to the very familiar form

$$\Delta^*\psi = -F(\psi)\frac{dF(\psi)}{d\psi} - \mu_0 R^2 \frac{\partial p(R,\psi)}{\partial \psi}. \tag{2.20}$$

Equation (2.20) is also shown from a slightly different approach in [7]. In fact, the isothermal Grad-Shafranov equation with toroidal flow is identical save for the presence of a partial derivative of the thermal pressure and the thermal pressure's R dependence. This limiting case is particularly useful for discerning regimes in which toroidal flow will make a significant difference in the equilibrium configuration. More specifically, toroidal flows comparable to the sound speed c_s will cause a notable shift in the mass density and thermal pressure profiles. The value of $M_\phi(\psi)$ for this particular limiting case is simply just the ratio

$$M_\phi(\psi) = \frac{2p_\omega(\psi)}{p_0(\psi)}, \tag{2.21}$$

where M_ϕ is a nominal toroidal Mach number proportional to the true toroidal Mach number, which will play an important role in determining how quickly the thermal pressure and mass density grow and decay.

Chapter 3

NIMEQ Results

3.1 Overview

In this chapter, we use NIMEQ to calculate equilibrium configurations and compare the static equilibria with the steady-state equilibria. Additionally, we will use FLOW to act as a benchmark for NIMEQ's new functionality and plot the percent difference between the two codes using the following equation

$$\% \text{ Difference } (R) = \frac{|X(R) - Y(R)|}{(X(R) + Y(R))/2} \times 100, \tag{3.1}$$

where X is a parameter from NIMEQ and Y is that same parameter from FLOW as a function of R. Equilibrium profiles will be expressed as a function of $\hat{\psi}$, where $\hat{\psi}$ is 0 at the magnetic axis and 1 at the edge. In each equilibrium, the $F(\hat{\psi})$, $p_0(\hat{\psi})$, and $D(\hat{\psi})$ models are not altered in anyway when comparing each equilibria's static and steady-state solution fields. The only difference come from the assignment of $\Omega(\hat{\psi})$, where $\Omega(\hat{\psi}) = 0$ when there is no flow. In an effort to establish a meaningful comparison between the high-β and low-β equilibriums, the peak value for the nominal toroidal Mach number $M_\phi(0)$ will be held constant.

It is important to note that (2.21) is the nominal toroidal Mach number, which means that like $p_0(\hat{\psi})$, $D(\hat{\psi})$, and $\Omega(\hat{\psi})$ the true toroidal Mach number is only equal to (2.21) at $R = R_0$ and in the trivial case when there is no flow. The relationship between the two Mach numbers is

$$M_\phi(R, \hat{\psi}) = \left(\frac{R}{R_0}\right) M_\phi(\hat{\psi}). \tag{3.2}$$

The difference between the peak values for the true and nominal versions can be minimal or significant depending on the static equilibrium configuration, especially in regards to the plasma shape. Since we wish to keep the Mach numbers the same between each equilibrium, we must determine the peak value for $\Omega(\hat{\psi})$ strictly from the nominal Mach number and fix the aspect ratio. Both equilibria have an aspect ratio $R_0/a = 2.86$ with $a = 1$m and $R_0 = 2.86$m, where a is the minor radius of the torus. Unpacking the nominal rotational pressure in (2.21) and solving for $\Omega(\psi)$ gives the equation that will be used to determine the peak toroidal flow:

$$\Omega(\hat{\psi}) = \frac{M_\phi(\hat{\psi})}{R_0}\sqrt{\frac{p_0(\hat{\psi})}{D(\hat{\psi})}}. \tag{3.3}$$

When calculating static equilibrium configurations, NIMEQ is not using its original routines to do the calculation. NIMEQ is programmed to take as input whether the equilibrium calculation should or should not use the isothermal Grad-Shafranov equation with toroidal flow to find the solution for the poloidal magnetic flux. This is done by changing the switch-like parameter in the NIMEQ input file to "noflow" or "toroidal". Setting this parameter to "noflow" uses the static version of the Grad-Shafranov equation, while setting it to "toroidal" uses (2.20). To better show agreement between NIMEQ and FLOW, the static equilibrium configurations are calculated by keeping the switch parameter set to "toroidal", but letting $\Omega(\hat{\psi}) = 0$.

As a final comment, it should be noted that FLOW always uses equations (2.13) and (2.14) to calculate each equilibrium configuration. We manually assign $\Phi(\hat{\psi}) = 0$ for all equilibria and $\Omega(\hat{\psi}) = 0$ for static equilibria. Since FLOW does not use the analytical expressions for thermal pressure and density for the isothermal limit, the isothermal limit is calculated by manually entering $\gamma = 1.000001$.

3.2 Low-β Tokamak Like Equilibrium

The first equilibrium configuration we will consider will be an equilibrium similar to that of a low-β tokamak. The profiles for $p_0(\hat{\psi})$, $F(\hat{\psi})$, $D(\hat{\psi})$, and $\Omega(\hat{\psi})$ are given by the following

Table 3.1: Coefficient values used for low-β tokamak like equilibrium configurations with and without toroidal flow. All values are in SI units.

Coefficient	$M_\phi = 0$	$M_\phi = .75$
p_0	121.59	121.59
p_1	91192.5	91192.5
f_0	9	9
f_1	9.6×10^{-2}	9.6×10^{-2}
f_2	6×10^{-3}	6×10^{-3}
Ω_0	10^{-4}	10^{-4}
Ω_1	0	159879.96
d_0	10^{-9}	10^{-9}
d_1	2.13×10^{-7}	2.13×10^{-7}

models:

$$p_0(\hat{\psi}) = p_0 + p_1\left(1 - \hat{\psi}\right) \tag{3.4}$$

$$F(\hat{\psi}) = f_0 + f_1\left(1 - \hat{\psi}\right) + f_2\left(1 - \hat{\psi}\right)^2 \tag{3.5}$$

$$\Omega(\hat{\psi}) = \Omega_0 + \Omega_1\left(1 - \hat{\psi}\right) \tag{3.6}$$

$$D(\hat{\psi}) = d_0 + d_1\left(1 - \hat{\psi}\right), \tag{3.7}$$

where the nominal values of p_0, p_1, p_2, f_0, f_1, f_2, Ω_0, Ω_1, d_0, and d_1 can be found in Table 3.1 and the peak poloidal flux and plasma parameters for each configuration can be found in Table 3.2. Peak values for parameters will be denoted with the subscript m and values at the magnetic axis will be denoted with subscript a. The equilibrium is defined by a large toroidal magnetic field, very low β_t, high q_*, and a relatively flat J_ϕ, where β_t is the ratio of thermal pressure to the toroidal magnetic pressure and q_* is the kink safety factor given by

$$q_* = \frac{a}{R_0}\sqrt{\frac{\beta_p}{\beta_t}}. \tag{3.8}$$

The parameter β_p is the poloidal analog to β_t.

The static J_ϕ profile, as shown by the black line in Figure 3.1's rightmost plot is not in fact completely uniform, but has a slight trough and crest to the left and right of the magnetic

Table 3.2: Peak poloidal magnetic flux and plasma parameters for the low-β tokamak like equilibrium. The ψ_a values are generated by NIMEQ, but the plasma parameters are calculated during the post-processing stage in FLOW. As of right now, NIMEQ does not have a means to accurately compute these parameters. These calculations do not affect the equilibrium profiles.

Parameter	$M_\phi = 0$	$M_\phi = .75$
ψ_a	.689	.695
q_*	2.297	2.299
β_t	1.16×10^{-2}	1.17×10^{-2}
β_p	1.14	1.13

axis. However, the toroidal current density can still be treated as effectively uniform since the deviation from a uniform profile is well within a 1% difference of a completely flat J_ϕ profile.

The $\Omega(\hat{\psi})$ profile for $M_\phi = M_\phi(R_m, \hat{\psi}_m)$ is constructed by first setting the nominal toroidal Mach number $M_\phi(\hat{\psi})$ to the desired value at $R = R_0$ in equation (3.3) to find the peak value of $\Omega(\hat{\psi})$. The value for Ω_0 is set very close to zero, but not exactly zero, as a means of providing minimal flow at the edge. The same is also done for the thermal pressure model's edge value in order to prevent $c_s \to 0$, which would cause a singularity in $M_\phi(R, \hat{\psi})$. Hence, it is technically more accurate to say $\Omega_1 = \Omega_a - \Omega_0$, but effectively $\Omega_a \approx \Omega_1$. Toroidal flow models for descending values of M_ϕ, with the exception of $M_\phi = 0$, are made by fixing Ω_0 and assigning each model's Ω_1 to 2/3, 4/9, and 1/3 of the original model's Ω_1.

The particle density profiles, as expected from our analytical expression for $\rho(R, \psi)$ in equation (2.19) and our quasi-neutral assumption, do indeed display a notable outward shift. In

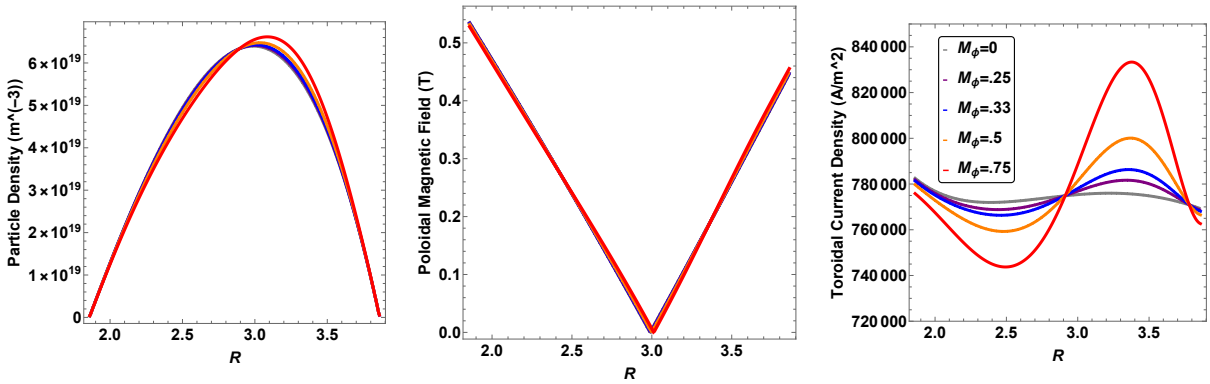

Figure 3.1: Midplane profiles for $n(R, \psi)$, B_p, and J_ϕ plotted as function of toroidal radius for increasing toroidal Mach number up to $M_\phi(R_m, \hat{\psi}_m) = .75$.

addition to the outward shift, the peak value itself exhibits as small increase. Note that in the isothermal limit, the closure relation defined by (2.10) requires that the thermal pressure have the exact same dependency as our particle density. Thus, the same axial and peak value shifts for increasing M_ϕ will apply for pressure as well.

On the other hand, the poloidal magnetic field is hardly affected by the increasing presence of toroidal flow, save for a very small shift of its vertex. For low-β equilibria, this result should be expected. From (2.12), the absence of poloidal flow means that $F(\psi) = RB_\phi$, which was also true in the static case. Since our B_ϕ profile is fixed the only way for B_p to deviate from the static case is if $\nabla\psi$ increases/decreases from the static equilibrium. Table 3.2 shows that increasing the toroidal Mach number at best changes the value of ψ_a by approximately .85%, which is roughly the same percent difference β_t and β_p experience as well. Additionally, $\beta_t \sim 1\%$ which is a direct result of the dominance of the magnetic pressure. Consequentially, the RHS of (2.20) will be dominated by the FF' term. Since the static and steady-state $F(\hat{\psi})$ models are identical, this means that even though the steady-state thermal pressure clearly deviates from its static form, the FF' term will still most likely dominate, barring incredibly high toroidal flow. Therefore, it is unlikely that $\nabla\psi$ will change much at all, which means neither will the poloidal magnetic field. We should expect that this will not be the case for the high-β equilibrium in the next section.

By looking at the J_ϕ profiles, as M_ϕ increases, it can be seen that the toroidal current is gradually pushed away from the geometric center of the poloidal cross-section of the torus. This is indicative of the centrifugal force contribution mentioned back in Chapter 2. Though the current pushed to the left of the geometric center seems to have its peak flipped, this is simply showing that the current density profile, whose non-uniformity we dismissed for the static equilibrium, is exacerbated by the increasing flow speed.

3.3 High-β Tokamak Like Equilibrium

The last equilibrium we will take a look at is similar to that of a high-β tokamak. The profiles for $p_0(\hat{\psi})$, $F(\hat{\psi})$, $D(\hat{\psi})$, and $\Omega(\hat{\psi})$ are given by the following models:

$$p_0(\hat{\psi}) = p_0 + p_1\left(1-\hat{\psi}\right) + p_2\left(1-\hat{\psi}\right)^2 \tag{3.9}$$

$$F(\hat{\psi}) = f_0 + f_1\left(1-\hat{\psi}\right) + f_2\left(1-\hat{\psi}\right)^2 \tag{3.10}$$

$$\Omega(\hat{\psi}) = \Omega_0 + \Omega_1\left(1-\hat{\psi}\right) \tag{3.11}$$

$$D(\hat{\psi}) = d_0 + d_1\left(1-\hat{\psi}\right), \tag{3.12}$$

where the nominal values of p_0, p_1, p_2, f_0, f_1, f_2, Ω_0, Ω_1, d_0, and d_1 can be found in Table 3.3 and the peak poloidal flux and plasma parameters for each configuration can be found in Table 3.4. The only change to plasma shape from that of the low-β equilibrium is the transition from a pressure that was linear in $\hat{\psi}$ to one that is slightly quadratic in $\hat{\psi}$ (as can be seen from the p_2 value in Table 3.3).

This equilibrium's defining features are the notably higher β_t, β_p, and J_ϕ, a weak toroidal magnetic field, and a linear J_ϕ profile corresponding to $\nu = .29$, where ν is the tokamak expansion parameter defined by $\nu = \beta_t q_*^2 R_0/a$. The coefficients for $p_0(\hat{\psi})$ and $F(\hat{\psi})$ were set to values that kept $\nu < 1/2$ [8]. For the sake of comparability with the low-β equilibrium, we

Table 3.3: Coefficient values used for high-β tokamak like equilibrium configurations with and without toroidal flow. All values are in SI units.

Coefficient	$M_\phi = 0$	$M_\phi = .75$
p_0	101.325	101.325
p_1	23026.4	23026.4
p_2	-948.19	-948.19
f_0	.99	.99
f_1	4.65×10^{-2}	4.65×10^{-2}
f_2	1.43×10^{-2}	1.43×10^{-2}
Ω_0	10^{-4}	10^{-4}
Ω_1	0	78795.51
d_0	10^{-9}	10^{-9}
d_1	2.13×10^{-7}	2.13×10^{-7}

Table 3.4: Peak poloidal magnetic flux and plasma parameters for the high-β tokamak like equilibrium.

Parameter	$M_\phi = 0$	$M_\phi = .75$
ψ_a	.2733	.2774
q_*	.651	.652
β_t	.2352	.2359
β_p	1.80	1.76

wish to keep our expansion parameter below the point at which we would start seeing a current reversal. Similar to before, inspection of the the static J_ϕ profile in Figure 3.2 reveals that it is not completely linear, but still effectively linear.

The particle density profiles do not display any significant deviation in shape, and only a slightly larger peak shift. Since $D(\hat{\psi})$ and $M_\phi(\hat{\psi})$ are the same models used in the low-β section, any change to the particle density profile would come from the shape of the thermal pressure. While the pressure is now technically quadratic in $\hat{\psi}$, it is still much closer to being linear since $p_2 << p_1$. Thus, the shift for the particle density is reminiscent of the shift seen in the low-β tokamak like equilibrium.

At first glance it may seem as though our prediction for the high-β equilibrium's B_p profile was wrong, but the difference here is somewhat subtle. Unlike before, the static poloidal field profile has a distinct bend on the left side of the vertex. The vertex does shift slightly more noticeably than with the low-β case, what is more interesting is that the steady-state profile bends the left side of the profile even more. As discussed in the last section, with our constraint

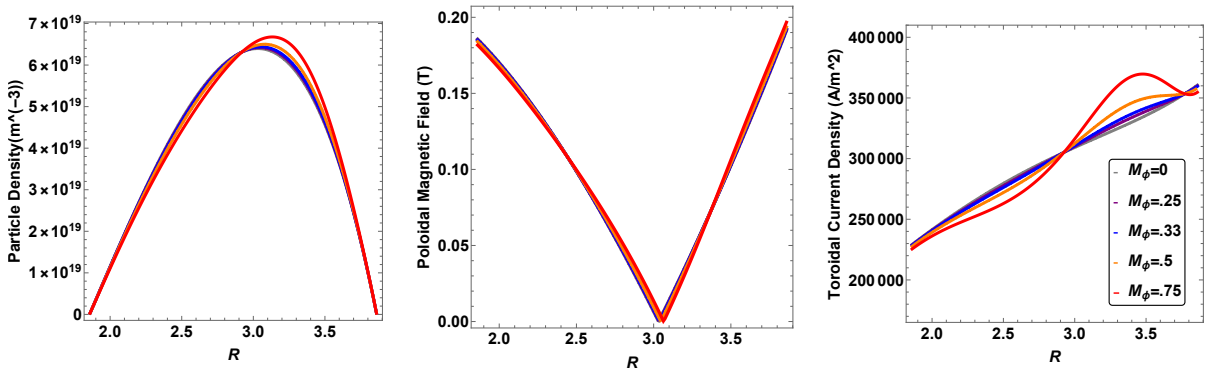

Figure 3.2: Midplane profiles for $n(R, \psi)$, B_p, and J_ϕ plotted as function of toroidal radius for increasing toroidal Mach number up to $M_\phi(R_m, \psi_m) = .75$.

on B_ϕ, B_p relies entirely on $\nabla\psi$. With the pressure term now dominant on the RHS of (2.20), as seen in Table 3.4, ψ_a changes by about 1.5% and β_p changes by about 2.25%.

Lastly, the J_ϕ profile in this configuration also shows the current being pushed away from the center, but in a different manner. More current is being pushed to the outer wall than towards the inner wall. While this can partly be explained by the non-uniformity of the static J_ϕ profile, J_ϕ's direct dependence on $\Delta^*\psi$ gives a more intuitive explanation. Once again, the dominance of the pressure term on the RHS is the main difference between this configuration and the last. In other words, it makes sense that the peak closest to the outer wall appears to take a shape similar to that of the pressure and density.

3.4 NIMEQ/FLOW Comparison

In this section we compare the equilibrium profiles for the low-β and high-β equilibria calculated by NIMEQ in the previous two sections with ones calculated by FLOW as a benchmark. More specifically, we will address the metrics used to determine the quality of the fits generated by both FLOW and NIMEQ and the percent difference for the particle density, poloidal magnetic field, and toroidal current density profiles.

Indicated back in the overview of this chapter, FLOW solves the (2.13) and (2.14) system of equations, while NIMEQ solves equation (2.20). NIMEQ uses a finite element approach to find a solution for ψ, while FLOW uses a multi-grid approach [1, 3]. For FLOW, each equilibrium calculation's merit was determined by increasing the number of iterations and final grid size until the solution for ψ at the center of the poloidal cross-section no longer varied. The residual was checked at each iteration of each grid to verify convergence. Similarly, NIMEQ's grid resolution and degree for the polynomial basis functions were independently increased until the solution ceased to deviate. Furthermore, two different tolerances are taken as input in for NIMEQ. The Grad-Shafranov equation's finite element representation can be represented in a form analogous to $Ax = b(x)$, where $x = \psi/R^2$, A is the Δ^* operator, and $b(x)$ is the RHS of the Grad-Shafranov equation. NIMEQ uses a modified Picard algorithm and iterates an equation of the form $Ax^n = b(x^{n-1})$, where each iteration requires an inversion of A. The first tolerance is used to control the accuracy of the inversion of A. The second tolerance is used to

determine when the nonlinear iterations (the inversion) has converged. The inversion tolerance and the nonlinear iteration convergence tolerance are set to 10^{-11} and 10^{-8}, respectively, for all equilibria.

Since, the two codes solve nearly identical equations for the limiting case of $\Omega(\psi) = 0$ and $\Phi(\psi) = 0$, the percent difference plots for this regime will provide a useful baseline for estimating the differences in the solution fields between the two codes. The toroidal magnetic field and poloidal current density profiles will be ignored since their static and steady-state forms are identical for purely toroidal flow. Since the grid points between codes are different, an interpolation is made of each equilibria's midplane profiles for each code. To mitigate interpolation error as much as possible, both FLOW and NIMEQ were given grid sizes with 257 data points. The percent difference for the low-β tokamak like equilibria are shown in Figure 3.3. One of the most immediate observations that can be seen in every plot in Figure 3.3 is the rapid oscillation in percent difference near the edges. This can be easily explained by noting the way NIMEQ handles open flux regions. NIMEQ somewhat crudely sets $\hat{\psi} = 1$ anywhere outside the the last closed flux surface [1]. Adjustments were made in FLOW's input file to match this, but FLOW will always require that the dimensions of the grid go slightly beyond this region [3]. In other words, FLOW will still assume some R dependence slightly past the closed flux region. However, in the static regime, it can be seen that the percent error drops dramatically once you move away from the edge.

The middle plots of Figure 3.3 show the percent difference for the poloidal magnetic field. While we noted earlier that the poloidal magnetic field deviates only slightly from the static equilibrium for low-β, it is still important to include since we will want to compare it with the percent error for the high-β equilibria. Additionally, the large spike in percent error that occurs even in the static limit is easier to understand in the low-β case. This spike is caused by the difference in the way each code assigns the value for the magnetic axis. FLOW assigns the magnetic axis by taking the radial grid point that contains the highest value of ψ. While for a sufficient number of grid points this is more than satisfactory, an interpolation between the adjacent grid points is a slightly more accurate way to find the exact point where the magnetic axis should be. As we saw in Figure 3.1, the poloidal field has a fairly steep slope on both sides

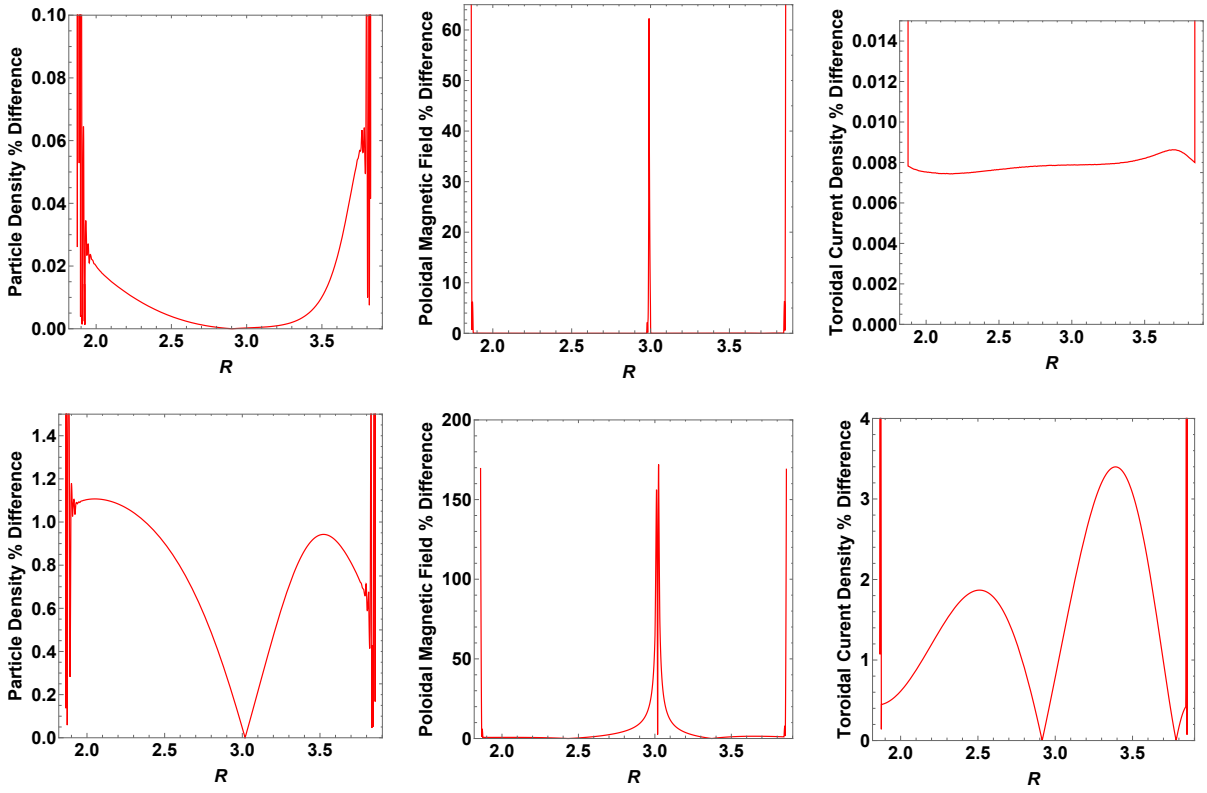

Figure 3.3: Percent difference plots for $n(R,\psi)$, B_p, and J_ϕ low-β equilibrium midplane profiles for the static case (top row) and the steady-state case with $M_\phi = .75$ (bottom row).

of its vertex. Even a small shift in the location of this vertex can lead to B_p in one code being almost twice the value of B_p in the other, hence the delta function like percent error about the magnetic axis. The width of the spike increases for flow since the percent difference for ψ will unsurprisingly marginally increase since the equations being solved are not identical.

For the moment we will hold off assessing the validity of the J_ϕ profiles. First we will look at the corresponding plots for the high-β equilibria as seen in Figure 3.4. Note that the plots all seem to have identical dependency on R, which is a good indication that the same metrics were used for all equilibria. The particle density and poloidal magnetic field plots' behavior is almost identical to their exhibited behavior in Figure 3.3.

The primary difference between FLOW and NIMEQ for both low-β and high-β lies in the calculation of the J_ϕ profile. Though the percent difference is reasonable, it is still substantially higher than it is for the other two profiles. As stated in the last section, the main difference comes from the increased influence of the pressure term in (2.20). While both codes determine J_ϕ from the RHS of their respective Grad-Shafranov equation, the Grad-Shafranov equation

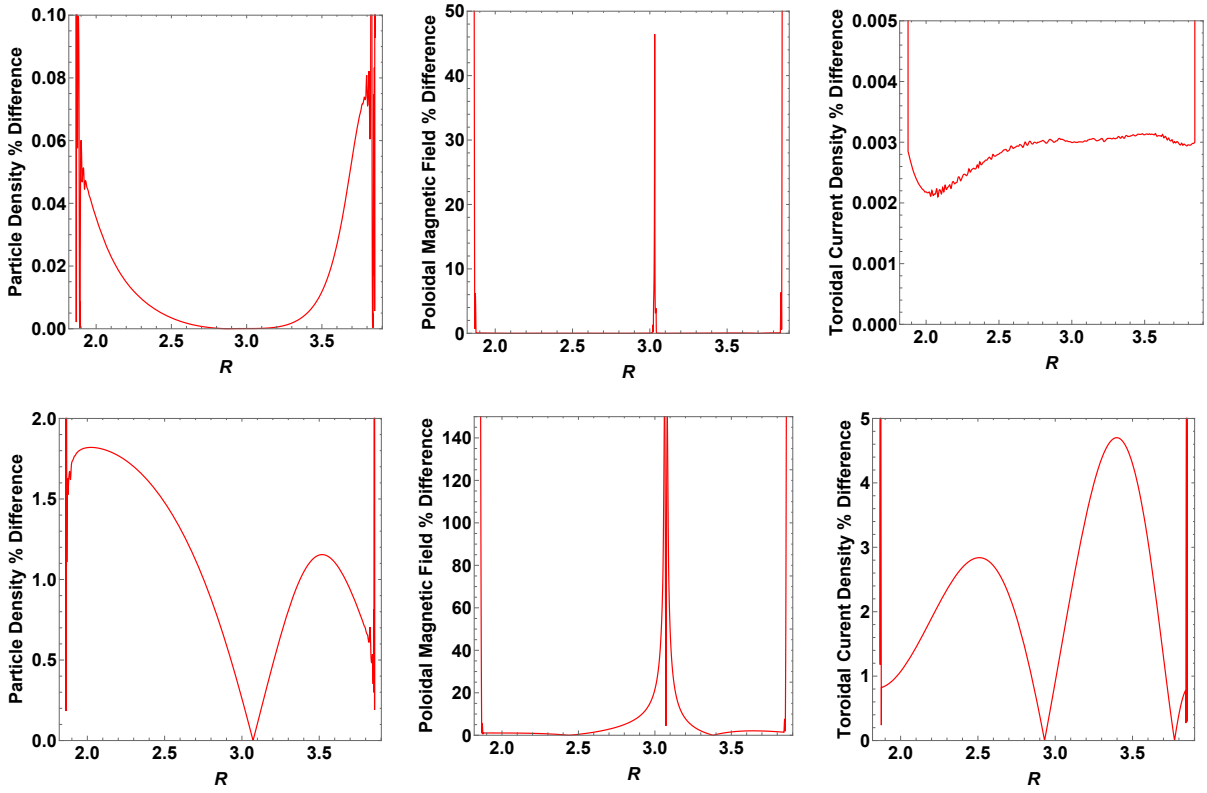

Figure 3.4: Percent difference plots for $n(R,\psi)$, B_p, and J_ϕ high-β equilibrium midplane profiles for the static case (top row) and the steady-state case with $M_\phi = .75$ (bottom row).

itself is not the same. FLOW must first solve for ρ using (2.17) in the isothermal limit. Noted back in the overview of this chapter, a value very close to one is used in order to prevent a singularity while solving for the density in equation (2.15). While NIMEQ uses the same value of γ, it is important to note that by using the analytical form of the thermal pressure (2.19), the only place where γ is used in calculating solution fields is when it calculates $S(\psi)$, which would never be able to cause a singularity. Additionally, the RHS of (2.20) has substantially fewer calculations that need to be made.

The plots in Figure 3.5 help to visualize this disparity. From these plots it is clear that the percent difference increases radially away from the center of the poloidal cross-section, with the greatest percent difference occurring at the maxima and minima of the profiles. Additionally, the agreement between NIMEQ and FLOW improves considerably towards the edge (barring the aforementioned open region difference). The percent difference even increases for the high-β equilibrium, as it should if the RHS is indeed to be the cause.

Figure 3.5: Comparison of FLOW and NIMEQ J_ϕ profiles for $M_\phi = .75$.

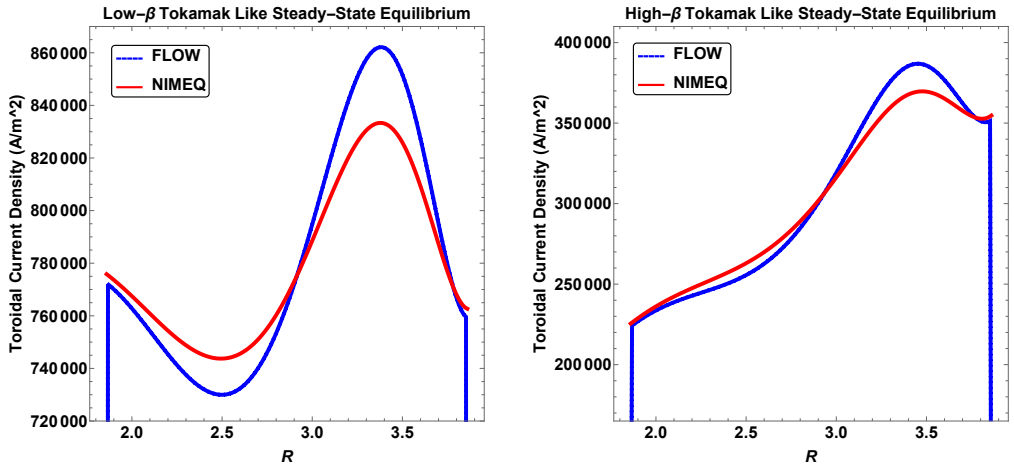

3.5 Conclusion

The effects of isothermal toroidal rotation have been shown to be significant in low and high β_t like tokamak configurations, with the most noteworthy addition to the static model being the rotational inertia pushing the toroidal current to the edge. The high-β tokamak like equilibria deviates more drastically from the static regime than the low-β like tokamak equilibria did. This result has been shown to be due to the larger pressure term on the RHS of the isothermal Grad-Shafranov equation with toroidal flow. These results are in good agreement with the code FLOW and the integration of flow into NIMEQ equilibrium calculations appears to have been successful.

With this special case implemented in NIMEQ, the next steps in developing this new functionality are to include purely toroidal flow and arbitrary flow options. For the purely toroidal flow Grad-Shafranov equation (2.16), this would mean adding a couple of terms to the RHS and residual integration routines in NIMEQ, as well a short routine used the calculate ρ at each iteration using (2.17). On the other hand, adding poloidal flow to NIMEQ would be a more challenging endeavor since (2.14) would need to be rearrange so that the LHS is $\Delta^*\psi$, which will introduce a $\nabla\psi/R^2$ term on the RHS. A routine/module would also need to be developed to solve the Bernoulli equation for the density. In addition to flow speeds comparable to the sound speed, when creating equilibria with poloidal flow, you must also pay attention to flow speeds comparable to the poloidal Alfvénic Mach number, as seen by the LHS of (2.14). The

addition of poloidal flow to the models used in this work, would likely alter the solution fields of low and high β tokamak like equilibria even further.

References

[1] C.R. Sovinec, A.H. Glasser, D.C. Barnes, T.A. Gianakon, R.A. Nebel, S.E. Kruger, D.D. Schnack, S.J. Plimpton, A. Tarditi, M.S. Chu and the NIMROD Team, "Nonlinear Magnetohydrodynamics with High-order Finite Elements," Journal of Computational Physics, **195**, 355 (2004).

[2] R. Betti and J. P. Freidberg, Phys. Plasmas **7**, 2439 (2000)

[3] L. Guazzotto, R. Betti, J. Manickam and S. Kaye, Phys. Plasmas **11**, 604 (2004).

[4] S. Semenzato, R. Gruber, and H. Zehrfeld, Comput. Phys. Rep. **1**, 389 (1984).

[5] A. J. Belien, M. A. Botchev, J. P. Goedbloed, B. van der Holst, and R. Keppens, J. Comput. Phys. **182**, 91 (2002).

[6] E. Hameiri, Phys. Fluids **26**, 230 (1983).

[7] S. Jardin, Computational Methods in Plasma Physics (Taylor & Francis, Boca Raton, FL, 2010).

[8] J. P. Freidberg, Ideal Magnetohydrodynamics (Plenum Press, Oxford, England, 1987).

Appendices

Appendix A

Finding the Poloidal Magnetic Field

The poloidal magnetic field is found by utilizing the the vector potential $\mathbf{A}$, where $\mathbf{B} = \nabla \times \mathbf{A}$. Note that the divergence of this magnetic field is already zero. We can relate the vector potential to the poloidal magnetic flux by using Stokes's Theorem, which yields

$$\psi_p = \int_{S_p} \mathbf{B} \cdot \mathbf{dS_p} = \oint \mathbf{A} \cdot \mathbf{dl_p}, \tag{A.1}$$

where S_p and l_p are the poloidal surface and the poloidal arc length. Thus, the poloidal flux is just $\psi_p = 2\pi R A_\phi$. Generally, we want to work instead with $\psi = \psi_p/2\pi = RA_\phi$ to minimize the number of coefficients carried throughout the derivation.

Taking the divergence of $\mathbf{B}$ in the case of axisymmetry, and substituting in our new expression for ψ, we get the following expressions for the R and Z components of the magnetic field:

$$\mathbf{B_R} = -\frac{1}{R}\frac{\partial \psi}{\partial Z}\hat{\mathbf{R}} \tag{A.2}$$

$$\mathbf{B_Z} = \frac{1}{R}\frac{\partial \psi}{\partial R}\hat{\mathbf{Z}}. \tag{A.3}$$

Note that the sum of these is $\mathbf{B_p}$ and looks very similar to $\nabla\psi$, which is given by

$$\nabla\psi = \frac{\partial \psi}{\partial R}\hat{\mathbf{R}} + \frac{\partial \psi}{\partial Z}\hat{\mathbf{Z}}. \tag{A.4}$$

In fact, taking $\nabla\psi \times \hat{\phi}$, noting that $\hat{\phi} = R\nabla\phi$, and comparing this to the sum of (A.2) and (A.3) gives us the expression we were looking for:

$$\mathbf{B_p} = \nabla\psi \times \nabla\phi. \tag{A.5}$$

Appendix B

Finding Velocity for Compressible Flow

To determine our expression for $\mathbf{v}$, we will use equations (2.1) and (2.5) which have been rewritten below:

$$\nabla \cdot (\rho \mathbf{v}) = 0 \tag{B.1}$$

$$\nabla \times (\mathbf{v} \times \mathbf{B}) = 0. \tag{B.2}$$

First we need to determine which basis vectors it can be written in terms of. Now that (B.2) implies that $\mathbf{v} \times \mathbf{B} = \nabla\alpha$, where α is an arbitrary scalar. This implies that $\mathbf{B} \perp \nabla\alpha$. The only way this is possible is if $\nabla\alpha \parallel \nabla\psi$. Since $\mathbf{v} \perp \nabla\alpha$, this means that our flow velocity does not have a $\nabla\psi$ component. Ergo, we can write $\mathbf{v}$ as

$$\mathbf{v} = C\nabla\psi \times \nabla\phi + Rv_\phi \nabla\phi, \tag{B.3}$$

where C is an arbitrary function (not necessarily a constant).

Substituting (B.3) into (B.2) and simplifying leads to the relationship

$$(\nabla\psi \times \nabla\phi) \cdot \nabla(\rho C) = 0, \tag{B.4}$$

which means $\nabla(\rho C) \perp \mathbf{B_p}$. Due to axisymmetry, it is impossible for $\nabla(\rho C)$ to be collinear with $\nabla\phi$, therefore it must be collinear with $\nabla\psi$. Therefore, we define a new function $\Phi(\psi)$ such that $C = \frac{\Phi(\psi)}{\sqrt{\mu_0}\rho}$. Finally, we substitute the newly updated $\mathbf{v}$ into (B.2) to get

$$\nabla\left[\frac{1}{R}\left(v_\phi - \frac{\Phi(\psi)}{\sqrt{\mu_0}\rho}\right)\right] \times \nabla\psi = 0. \tag{B.5}$$

Equation (B.5) once again tells us that the term in the brackets must be another free function that we will call $\Omega(\psi)$. Rearranging and solving for v_ϕ yields

$$v_\phi = \frac{\Phi(\psi)}{\sqrt{\mu_0}\rho} B_\phi + R\Omega(\psi). \tag{B.6}$$

Now all that needs to be done is to recombine the two components to get our final expression for the flow velocity:

$$\mathbf{v} = \frac{\Phi(\psi)}{\sqrt{\mu_0}\rho}\mathbf{B} + R^2\Omega(\psi)\nabla\phi. \tag{B.7}$$

Appendix C

The $\nabla\phi$ Component of the Momentum Equation

The $\nabla\phi$ component of the momentum equation is given by

$$\nabla\phi \cdot (\rho\mathbf{v} \cdot \nabla\mathbf{v}) = \nabla\phi \cdot (\mathbf{J} \times \mathbf{B}) \,. \tag{C.1}$$

Upon substituting $\mathbf{J}$ and $\mathbf{B}$ into (C.1), our expression reduces to

$$\nabla\phi \cdot [\mathbf{v} \times (\nabla \times \mathbf{v})] = \frac{1}{\mu_0 \rho R^2} \left(\nabla \left(RB_\phi\right) \times (\nabla\phi \cdot \nabla\psi)\right). \tag{C.2}$$

First start by simplifying the LHS of (C.2) by plugging in our expression for $\mathbf{v}$ and putting the resulting expression in terms of $\nabla\psi \times \nabla\phi$ dotted with a scalar gradient. Doing so results in the LHS's expression being

$$\nabla\phi \cdot [\mathbf{v} \times (\nabla \times \mathbf{v})] = -\frac{\Phi(\psi)}{\sqrt{\mu_0}\rho R^2} \left(\nabla\psi \times \nabla\phi\right) \cdot \nabla \left(\frac{\Phi(\psi)}{\sqrt{\mu_0}\rho} RB_\phi + R^2\Omega(\psi)\right). \tag{C.3}$$

Now that both sides of (C.2) can be expressed in terms of our basis vectors and scalar quantities, inserting (C.3) into (C.2) yields the desired expression:

$$\left(\nabla\psi \times \nabla\phi\right) \cdot \nabla \left(\frac{\Phi(\psi)^2}{\rho} RB_\phi + \sqrt{\mu_0} R^2 \Phi(\psi)\Omega(\psi) - RB_\phi\right) = 0. \tag{C.4}$$

The nice thing about (C.4) is that all RB_ϕ terms are conveniently located inside the scalar gradient (so RB_ϕ will be able to be solved for in very much the same way as in the static case, but with additional terms. Equation (C.4) implies that the scalar gradient must be collinear with $\nabla\psi$ and thusly the scalar inside the gradient must be a free function of ψ, which we will call $F(\psi)$ for the sake of comparison with the static regime. Solving for RB_ϕ we get the final expression:

$$RB_\phi = \frac{F(\psi) + \sqrt{\mu_0} R^2 \Phi(\psi)\Omega(\psi)}{1 - \Phi(\psi)^2/\rho}. \tag{C.5}$$

Appendix D

The $\mathbf{B}$ Component of the Momentum Equation

The field alligned component of the momentum equation is given by

$$\mathbf{B} \cdot (\rho \mathbf{v} \times \nabla \mathbf{v}) + \mathbf{B} \cdot \nabla p = 0. \tag{D.1}$$

It is easiest to take this one term at a time and try and put the expression for each term in the form of a dot product of a scalar gradient and $\nabla\psi \times \nabla\phi$. Doing so for both terms gives us:

$$\mathbf{B} \cdot (\rho \mathbf{v} \times \nabla \mathbf{v}) = (\nabla\psi \times \nabla\phi) \cdot \rho \nabla \left[\frac{v^2}{2} - \left(\frac{\Phi(\psi)\Omega(\psi)}{\sqrt{\mu_0}\rho} R B_\phi + R^2 \Omega(\psi)^2 \right) \right] \tag{D.2}$$

$$\mathbf{B} \cdot \nabla p = \left(\frac{\gamma}{\gamma - 1} \right) (\nabla\psi \times \nabla\phi) \cdot \rho \nabla \left(\rho^{\gamma - 1} S(\psi) \right). \tag{D.3}$$

The $v^2/2$ is unexpanded mainly for the sake of compactness, but this term is also helpful in spotting the Bernoulli equation that comes out of this component of the momentum equation. Additionally, the thermal pressure has been expressed in terms of the density and $S(\psi)$.

Recombining (C.1) and (C.2) results in another expression that requires the creation of a free function, which is

$$(\nabla\psi \times \nabla\phi) \cdot \rho \nabla \left[\frac{v^2}{2} - \left(\frac{\Phi(\psi)\Omega(\psi)}{\sqrt{\mu_0}\rho} R B_\phi + R^2 \Omega(\psi)^2 + \left(\frac{\gamma}{\gamma - 1} \right) \rho^{\gamma - 1} S(\psi) \right) \right]. \tag{D.4}$$

The term inside the hard brackets is a Bernoulli equation which we will set equal to the free function $H(\psi)$. Therefore, our Bernoulli equation can be simplified to the form:

$$\frac{1}{2\mu_0} \left(\frac{\Phi(\psi) B}{\rho} \right)^2 - \frac{1}{2} R^2 \Omega(\psi)^2 + \left(\frac{\gamma}{\gamma - 1} \right) \rho^{\gamma - 1} S(\psi) = H(\psi). \tag{D.5}$$

Appendix E

The $\nabla\psi$ Component of the Momentum Equation

The $\nabla\psi$ component of the momentum equation is given by:

$$\nabla\psi \cdot (\rho\mathbf{v} \cdot \nabla\mathbf{v}) = \nabla\psi \cdot (\mathbf{J} \times \mathbf{B}) - \nabla\psi \cdot \nabla p. \tag{E.1}$$

We will take each term in (E.1) one at a time. Note that the LHS of (E.1) can be rewritten as

$$\nabla\psi \cdot (\rho\mathbf{v} \cdot \nabla\mathbf{v}) = \rho\nabla\psi \cdot \left[\nabla\left(\frac{v^2}{2} - \mathbf{v} \times (\nabla \times \mathbf{v})\right)\right]. \tag{E.2}$$

We leave (E.2) in this unexpanded form due to the redundancy of the $\mathbf{v} \times (\nabla \times \mathbf{v})$ term on the RHS. This expression would have been found back in the derivation for the $\nabla\phi$ component of the momentum equation in Appendix C. The other two terms on the RHS of (E.2) become:

$$\nabla\psi \cdot (\mathbf{J} \times \mathbf{B}) = \frac{1}{\mu_0 R^2}\left[\left(\frac{2}{R}\frac{\partial\psi}{\partial R} - \nabla^2\psi\right)|\nabla\psi|^2 - \nabla\psi \cdot \nabla\left(\frac{R^2 B_\phi^2}{2}\right)\right] \tag{E.3}$$

$$\nabla\psi \cdot \nabla p = \rho^\gamma \frac{dS(\psi)}{d\psi}|\nabla\psi|^2 + \gamma\rho^{\gamma-1}S(\psi)\nabla\psi \cdot \nabla\rho. \tag{E.4}$$

Now that all of the terms for (E.1) have been assembled, the time has come to finally derive the Grad-Shafranov equation for arbitrary flow. However, before doing so, two mathematical tricks should be noted, as they are crucial to the rest of the derivation. The first one is the simplest: $\nabla\psi \cdot \nabla F(\psi) = F'(\psi)|\nabla\psi|^2$, where the prime indicates a derivative with respect to ψ. It is worth noting that this trick works for the other free functions as well. The second trick is to write any $v^2/2$ terms in terms of $H(\psi)$. This results in the useful substitution

$$\frac{v^2}{2} = H(\psi) + \frac{\Phi(\psi)\Omega(\psi)}{\sqrt{\mu_0\rho}}RB_\phi + R^2\Omega(\psi)^2 - \left(\frac{\gamma}{\gamma-1}\right)\rho^{\gamma-1}S(\psi). \tag{E.5}$$

Using the aforementioned tricks, grouping all of the terms together on one side, and dividing out the common factor of $|\nabla\psi|^2$, we find that the $\nabla\psi$ component of the momentum equation reduces to

$$\rho\frac{dH(\psi)}{d\psi} - \frac{\rho^{\gamma-1}}{\gamma-1}\frac{dS(\psi)}{d\psi} + \frac{1}{\mu_0}\nabla \cdot \left[\left(1 - \frac{\Phi(\psi)^2}{\rho}\right)\frac{\nabla\psi}{R^2}\right] + \frac{\Phi(\psi)}{\mu_0\rho}\frac{d\Phi(\psi)}{d\psi}\frac{|\nabla\psi|^2}{R^2} \tag{E.6}$$

$$+\frac{\Phi(\psi)}{\sqrt{\mu_0}}RB_\phi\frac{d\Omega(\psi)}{d\psi}+\rho R^2\Omega(\psi)\frac{d\Omega(\psi)}{d\psi}+\left(\frac{B_\phi}{\mu_0 R}\right)\frac{dF(\psi)}{d\psi}+\frac{\Phi(\psi)}{\mu_0\rho}\frac{d\Phi(\psi)}{d\psi}B_\phi^2$$
$$+\frac{\Omega(\psi)}{\sqrt{\mu_0}}RB_\phi\frac{d\Phi(\psi)}{d\psi}=0.$$

There is one last trick that is needed to get our Grad-Shafranov equation. Once all of the terms in (E.6) have been grouped by common free function derivative (i.e. group all of the $\Phi'(\psi)$ and $\Omega'(\psi)$ terms), the final thing to notice is that the expression in front of the $\Phi'(\psi)$ term is just $\mathbf{v}\cdot\mathbf{B}$. Hence, the Grad-Shafranov equation for arbitrary flow is given by

$$\begin{aligned}\frac{1}{\mu 0}\nabla\cdot\left[\left(1-M_{Ap}^2\right)\left(\frac{\nabla\psi}{R^2}\right)\right]=&\frac{B_\phi}{\mu_0 R}\frac{dF(\psi)}{d\psi}-\frac{\mathbf{v}\cdot\mathbf{B}}{\sqrt{\mu_0}}\frac{d\Phi(\psi)}{d\psi}-\rho R v_\phi\frac{d\Omega(\psi)}{d\psi}\\&-\rho\frac{dH(\psi)}{d\psi}+\frac{\rho^\gamma}{\gamma-1}\frac{dS(\psi)}{s\psi},\end{aligned}\tag{E.7}$$

where $M_{Ap}=\Phi(\psi)/\sqrt{\rho}$ is the poloidal Alfvénic Mach number.